

# Experimental Route to Scanning Probe Hot-Electron Nanoscopy (HENs) Applied to 2D Material

Andrea Giugni, Bruno Torre, Marco Allione, Gobind Das, Zhenwei Wang, Xin He, Husam N. Alshareef, and Enzo Di Fabrizio\*

This paper presents details on a new experimental apparatus implementing the hot electron nanoscopy (HENs) technique introduced for advanced spectroscopies on structure and chemistry in few molecules and interface problems. A detailed description of the architecture used for the laser excitation of surface plasmons at an atomic force microscope (AFM) tip is provided. The photogenerated current from the tip to the sample is detected during the AFM scan. The technique is applied to innovative semiconductors for applications in electronics: 2D MoS<sub>2</sub> single crystal and a p-type SnO layer. Results are supported by complementary scanning Kelvin probe microscopy, traditional conductive AFM, and Raman measurements. New features highlighted by HEN technique reveal details of local complexity in MoS<sub>2</sub> and polycrystalline structure of SnO at nanometric scale otherwise undetected. The technique set in this paper is promising for future studies in nanojunctions and innovative multilayered materials, with new insight on interfaces.

## 1. Introduction

The recent availability of nanostructures of different types has promoted the fast development of new enhanced spectroscopies. The reasons are mainly related to the intrinsic nature of the surface plasmon polariton (SPP) that relies on surface charge density fluctuation at optical frequencies, whose propagating or localized character depends on the architecture of the nanostructure and the relative boundary conditions. What emerges from the nature of the SPP is that the length scale of this excitation is only determined by the size and shape of the structures.<sup>[1]</sup> In other words, the localization of an SPP is not limited by diffraction.<sup>[2]</sup> This peculiar characteristic moves the skill of the designer toward the miniaturization and the

fabrication ability of novel nanostructures where the relevant aspect is the exploitation and the understanding of the way to control of energy localization.

An important aspect directly derived from the dual nature of SPPs is the existence of two different decay channels, photons and hot carriers, whose relative contribution can be engineered in proximity of edges and apexes.<sup>[3,4]</sup> From the experimental point of view, this opens to the possibility of realizing concurrent optical and transport enhanced spectroscopies confined in a nanometric volume.

Our efforts are dedicated to integrate plasmonic nanostructures with atomic force microscopes (AFM), specifically designing cantilevers with a built in plasmonic nanotip,<sup>[5]</sup> like the one shown in Figure 2c. Among various plasmonic


metals,<sup>[6,7]</sup> we considered gold for its chemical stability and optimal electrical conductivity. The modified cantilevers preserve their original functions as mechanical probes for topography and force measurements and allow new optical and transport capabilities, generated by the SPPs dual decay. We use a plasmonic grating coupler to excite the SPPs along the tip, while a conical probe end permits the SPPs adiabatic compression that guarantees a high signal to noise ratio and high spatial resolution, both defined by the radius of curvature of the tip itself.<sup>[8–13]</sup> This approach inherits all the advantages of the scanning probe technique, i.e., the accurate control of tip-sample relative position and interaction, and allows accurate optical and transport measurements by the integration of spectrometers and current detection setups.

A comprehensive theoretical description of the phenomena supporting the efficient hot charges generation at the apex of a plasmonic tip,<sup>[4,11,14,15]</sup> along platelets,<sup>[4]</sup> or in thin films of plasmonic metals<sup>[16]</sup> can be found in the dedicated literature,<sup>[5]</sup> which already has proposed several relevant applications.<sup>[3,9,17–20]</sup> Here we focus on the basic ideas leading to a good hot carrier generation rate as result of SPPs propagation along a conical shaped tip in adiabatic compression.

The adiabatic compression description<sup>[11,12]</sup> is based on nonstrictly necessary optical and geometrical hypotheses that make it one of the possible models that explain the superfocusing effect.<sup>[9,13,21]</sup> Nevertheless, it is extremely explicative because it addresses the core of the phenomenon. The geometrical constraint arises from the assumption of the eikonal

Dr. A. Giugni, Dr. B. Torre, Dr. M. Allione, Dr. G. Das, Prof. E. Di Fabrizio  
King Abdullah University of Science and Technology (KAUST)  
Physical Sciences and Engineering Division (PSE)  
Thuwal 23955-6900, Saudi Arabia  
E-mail: enzo.difabrizio@kaust.edu.sa

Z. Wang, X. He, Prof. H. N. Alshareef  
King Abdullah University of Science and Technology (KAUST)  
Materials Science and Engineering Division (MSE)  
Thuwal 23955-6900, Saudi Arabia

 The ORCID identification number(s) for the author(s) of this article can be found under <https://doi.org/10.1002/adom.201700195>.

DOI: 10.1002/adom.201700195

approximation, also known as Wentzel–Kramers–Brillouin approximation, which limits the grading of the structure, while optically TM modes are required. Through the propagation, the effective wavelength, the group velocity, the refractive index, and the radial electric field of SPPs undergo the adiabatic compression in the material producing the ultimate focusing effect. In particular, as the apex is approached by the plasmonic wave, the refractive index  $n$  increases as  $1/R$  along the taper,<sup>[12]</sup> the effective wavelength of the SPP decreases asymptotically to zero according to the expression  $\lambda = \lambda_0/n(R)$ , as also the phase and the group velocity do, in fact  $v_p = c/n(R)$ ,  $v_g = c/[d(n(R)\omega)/d\omega]$ . This effect avoids the diffraction and permits the continuous focusing, with a concurrent increase in the local field amplitude, as well as in the average energy of the generated hot carriers. In addition, we note that the SPP skin depth scales down with the local taper radius, meaning that the maximal confinement occurs just at the metal-dielectric interface at the apex, with a behavior quite different from what observed for plasmonic thin films. For example, for gold at  $\lambda = 630$  nm the bulk SPP skin depth is  $\approx 13$  nm, while it can rescale several times down to few nm reaching the apex. Conversely, a nonplasmonic waveguide, i.e., a conventional tapered optical fiber, supports guided photonic modes up to a limiting minimum core size, and then there is a wavelength dependent cutoff. These results are the core of the adiabatic compression.<sup>[22]</sup> Thus, we believe that promoting adiabatic compression leads to a maximal benefit from the experimental point of view, when transport or spectroscopic investigation at the nanoscale is required.

In the paper, we report a new set up at SMILEs lab dedicated to hot electrons ( $he$ ) measurements. Specifically, we want to highlight the capability to keep the optical energy concentrated on the nanoscale thanks to SPPs by focusing it progressively to the tip. Energy concentration and nanoconfinement allow to damp out efficiently the SPPs and to generate a suitable high energy distribution of carriers.<sup>[4]</sup> The hot electron can be detected without the need of any external bias according to the effect of the diode rectification in a Schottky barrier when a gold metallized tip is set in contact with the sample<sup>[14,18]</sup> (see the electric scheme of Figure S5b of the Supporting Information). The strong localization of SPPs decay in the nanosized volume of the tip realizes a point current source of  $he$  confined at the interface with the sample. This behavior is quite different from that of the Ohmic contact where the current is proportional to the applied potential difference or with respect to the junction diodes where, to energize the electrons, the applied potential also strongly modifies the depletion region extension. The  $he$  current measurement will primarily be sensitive to the local variation of transport properties or band structures, and reveals the chemical and structural variation of the sample at the nanoscale.

The same setup allows the integration of additional traditional measurements, such as scanning Kelvin probe microscopy (SKPM) and  $I$ - $V$  spectroscopy.

In the following, we present details on the set up and the results of hot electrons measurement on a real device consisting of a recently proposed p-n junction based on a novel SnO/MoS<sub>2</sub> architecture, revealing new local features in the surface states.

## 2. Surface Plasmon Polariton Generation

An SPP<sup>[23]</sup> is a bosonic quasiparticle that exists at the interface between a metal and a dielectric medium and can be excited by the photon energy absorption process. It describes the nonequilibrium collective excitation of the free electron gas at the metal surface, coupled with the electromagnetic field, as stated in the Fano resonant model.<sup>[24]</sup>

The momentum mismatch between the SPP and the photon prevent the direct decoupling to far field radiation that motivates the appellation of “dark modes” for SPPs. These properties result in an exceptionally long mean free propagation length for the SPPs when compared to that of a single electron, which is of few tens of nm.

The large propagation lengths of SPPs, typically tens of micrometers for the case of noble metals like gold and silver in the visible to IR region, has been attracting the attention in photonic progressively as well as in electronic research fields.<sup>[14,25–27]</sup> The realization of an efficient unidirectional coupler for SPPs, in fact, allows controlling energy transport mediated by electric charges density fluctuation with the external optical field, with ultimate bandwidth and minimal dissipation, and is at the base of an overall efficient hot electrons generation.<sup>[3,4]</sup>

An important experimental aspect in the generation of SPPs is the optimization of the coupling between the photons source and the metal nanostructure, where the SPPs will be generated and eventually conveyed to a specific space location. In our application, it is important that during this process a consistent portion of the photons is converted in SPPs and redirected towards the tip.

Grating couplers are the leading solution to achieve nanosized bright hotspots and hot carriers source probes either for continuous wave or pulsed broadband lasers.<sup>[28,29]</sup> Here we focus the attention on the practical case we studied to optimize a grating to be matched with a commercial AFM probe tip. We realized a diffraction grating consisting of a finite size periodic modulation of a metallic surface realizable by focused ion beam milling and evaporation processes. According to the tip shape and the scattering geometry adopted, the grating was optimized taking into account the optimal illumination position and the minimization of the losses within the grating itself, once a specific Gaussian beam of predetermined waist was generated by the illuminating optics. In general, the finite size of the AFM tip allows to accommodate a small number of grooves. On one side, the limited number of grooves reduces the maximal coupling efficiency obtainable with respect to the classical optical grating case, on the other, it allows to diffract a broad frequency range into SPPs as shown in **Figure 1c**. This, for example, is a property that can be particularly useful when dealing with pulsed sources.

We imposed a further design constraint by choosing an optical geometry where the specular reflection of the incoming beam propagated far from the sample, leaving only the SPP propagating toward the sample. This design is particularly suitable for high S/N ratio in spectroscopic applications.

The trade-off of the plasmonic losses along the grating surface and the local coupling strength maximizes the SPP generation efficiency. From the optical point of view, this is the most relevant difference between a SPP launcher and a photon

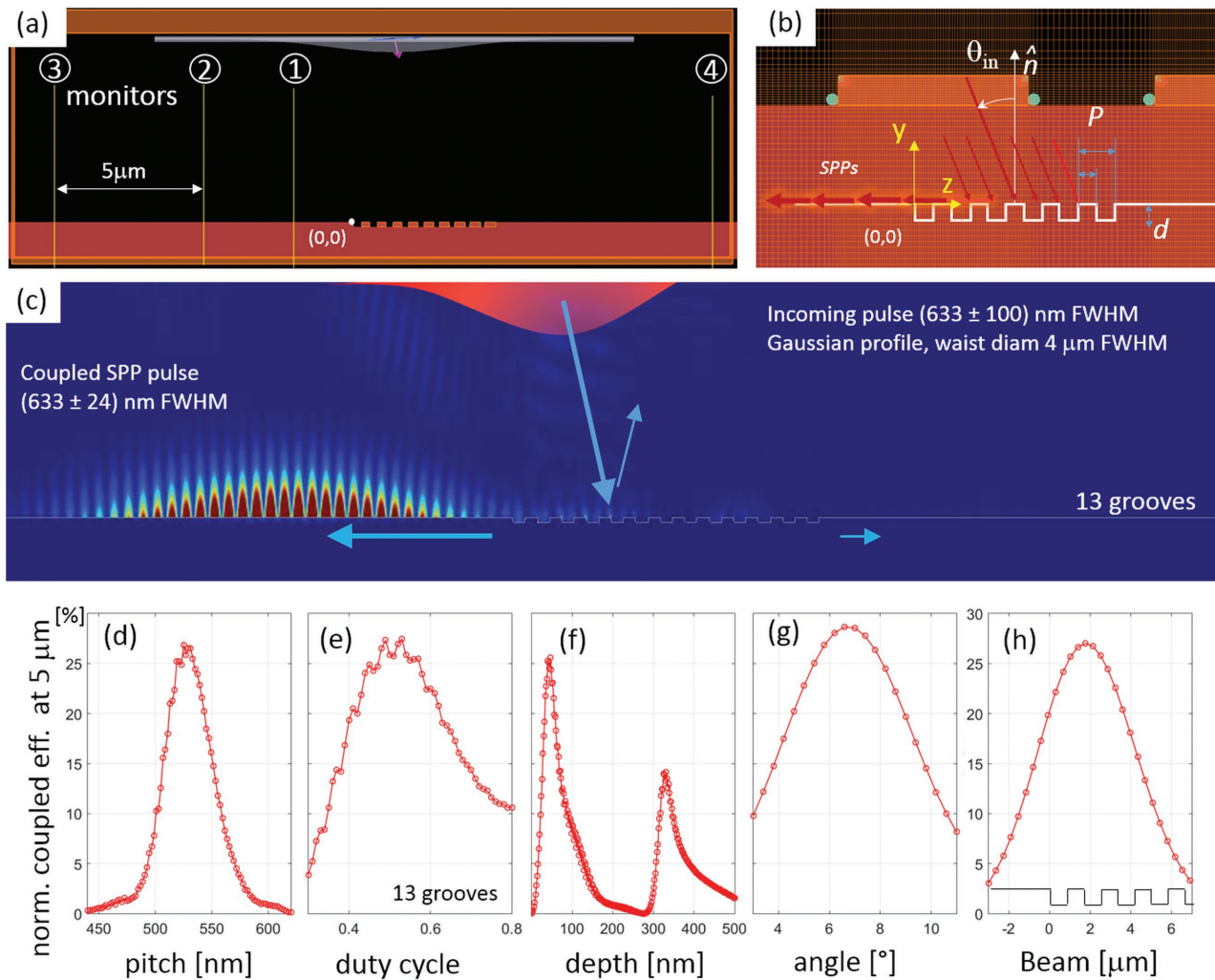


**Figure 1.** a) Representative FDTD snapshot of the simulated computational window and the grating geometry including the four monitors used for the energy flux, indicated as vertical lines. b) It is shown a detail of the mesh refinement used to match the grooves sizes, and highlighted the 20 nm rounded curvature of edges (see also Figure S1a,b, Supporting Information). A sketch of the scattering geometry and the five free parameters of the simulation is indicated. c) Snapshot of the propagating SPPs pulse along the metal surface, evidencing the unidirectional character. Arrows indicate the main directions of the power flow. Due to the bandpass nature of the grating, only a certain amount of spectral intensity is allowed to couple into SPPs. d–h) Power at 633 nm measured as energy flow across monitor #2, normalized on the coupled one as a function of the groove pitch, duty cycle, groove depth, incidence angle of the simulated Gaussian beam, and beam axis position with respect to the (0,0) coordinate indicated in (b), respectively.

diffraction grating. We add further details of this optimization study in Section S1 of the Supporting Information.

Considering the scattering geometry sketched in Figure 1b, the simple rule for the selection of grating pitch  $P$  arises from the momentum matching condition

$$\frac{2\pi}{P} = K_z^{\text{SPP}} - K_z^{\text{ph}} = \frac{\omega}{c} \sqrt{\frac{\epsilon_d \epsilon_m}{\epsilon_d + \epsilon_m}} - \frac{2\pi}{\lambda} \sin \theta_{\text{in}} \quad (1)$$

being  $\lambda$  the free space wavelength,  $z$  the SPP propagation direction,  $\theta_{\text{in}}$  the incidence angle, and  $\epsilon_d$  and  $\epsilon_m$  the frequency-dependent permittivity of the dielectric and the metal material, respectively.<sup>[30,31]</sup> However, a rigorous solution of the matching problem is not trivial, since the  $K_z^{\text{SPP}}$  in the grating region has a dependence on all the grating parameters, including  $P$ .

We considered a TM polarized 1D focused Gaussian beam profile having a waist width of 4  $\mu\text{m}$  full width at half maximum (FWHM), typical for a low NA lens, with a free-space wavelength  $\lambda_0 = 633$  nm and an incident angle of  $\theta_{\text{in}} = 6.7^\circ$  with respect to the normal of the surface and opposite to SPPs propagation direction. This particular configuration describes the mild back propagation of the SPP for a specific condition of our interest used in the experimental section. A second optimization was repeated for a different incidence angle to investigate the optimized backscattering geometry, and also for different type of AFM tip, a pyramidally shaped  $\mu$ -mash CSC38 type, to investigate the maximum coupling efficiency in the case of thin/transparent samples when illuminating the tip from the bottom using an inverted microscope.

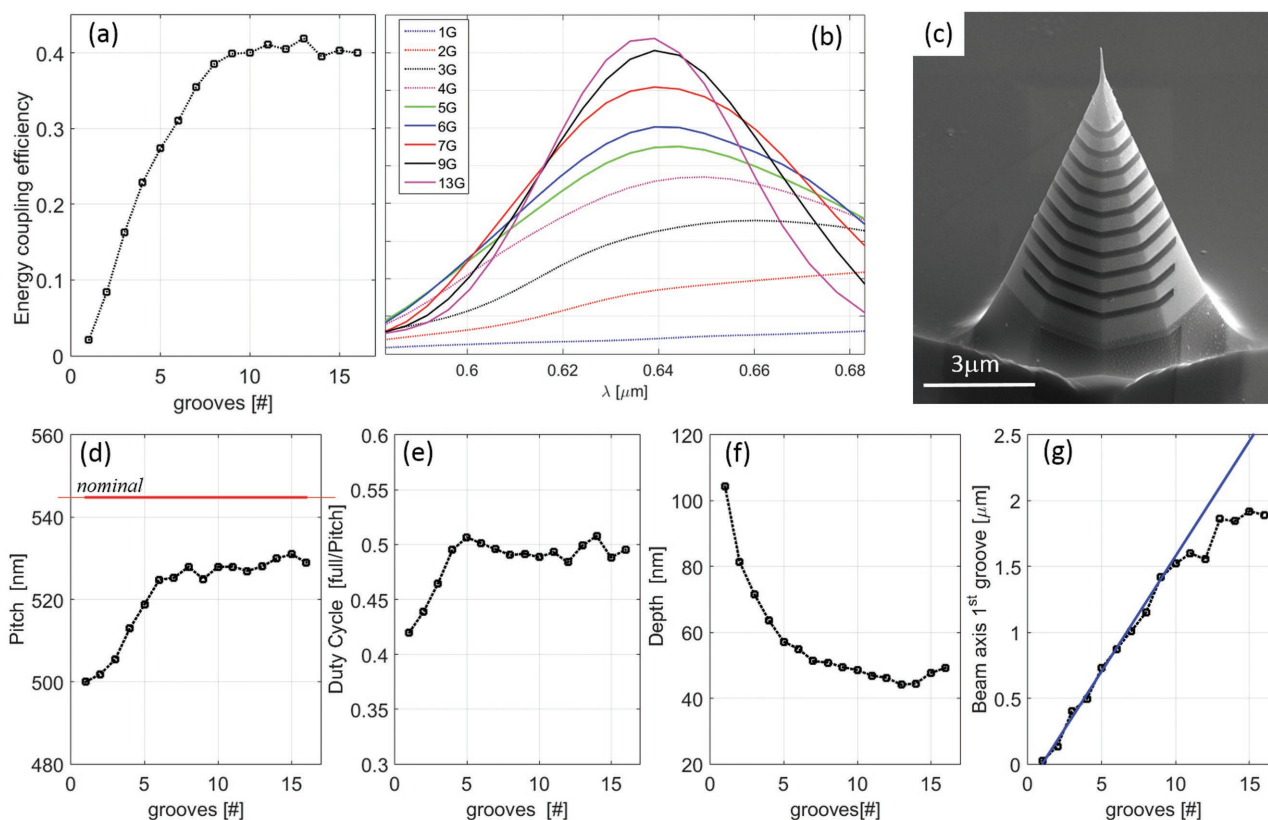


**Figure 2.** a) Relative coupling efficiency with respect to the incoming laser power as a function of the groove number. b) Spectral response of the grating for different groove number. c) SEM image of an example of microfabricated tip. d) Pitch, e) duty cycle, f) depth, g) position of the incident beam with respect to the first groove as a function of the groove number for an incident Gaussian beam. The excitation wavelength is 633 nm.

Within this scattering geometry, a uniform plasmonic grating launcher can reach a unidirectional efficiency up to 40%, as shown in **Figure 2a** already for a grating with less than ten grooves. We used the finite-difference time-domain (FDTD) method to model the grooves and simulate their performances as a function of their geometrical parameters.

Considering the achievable fabrication tolerances and abilities, we chose to modulate the grating by allowing varying locally the duty cycle and the pitch. In this way, simply adding a linear dependence on these parameters with respect to the position we get a further improvement larger than 5%, as shown in **Figure S3** of the Supporting Information.

We have also investigated the SPPs coupling by means of grating realized with an array of gold nanowires deposited on a silicon substrate. We report the case of an optimized array in **Figure S3** of the Supporting Information comparing it with the full metallic grating, to highlight the nonstrictly necessity of the continuity of the metal and the different optimal depths required in the two cases. We highlight that the groove top-surface plays the most important role in launching SPPs. The retarded wave propagating along the groove depth and reflected back to the surface contributes to the total intensity with a modulation term, with a maximal contribution for a phase delay that results in a trade-off between constructive interference phenomenon and SPP damping, similar to the dielectric case.<sup>[32]</sup>

Frequency-dependent real and imaginary permittivity components of gold, the metal used in the simulations, were taken

from recent literature results,<sup>[30]</sup> while the refractive index of the air was set to  $n = 1$ . As shown in **Figure 2**, considering a Gaussian beam and the mild backscattering geometry, we have evaluated the optimal parameters for the coupling under an increasing number of grooves starting from the single slit case. We found that, with increasing of the number of grooves, all parameters converge to characteristic values for the scattering geometry. For the smaller numbers, the single slit behavior dominates,<sup>[33,34]</sup> while for a sufficiently large number, more than 6, the grating character prevails. This is highlighted also by the shallowing of the depth parameter that reaches the expected optimal value for a grating, and by the spectral shape of the coupled energy in SPP, as shown in the graphs of **Figure 2**, and **Figure S2** (Supporting Information). As expected, also the position of the light beam on the grating has a defined dependence on the groove number that derives from the trade-off between the number of scattering centers excited and the SPP damping factor modulated by the grating length.

For the case of 13 equally spaced grooves reported in **Figure 1c** (total grating length  $< 7 \mu\text{m}$ ), we identified the optimal parameters: pitch, duty cycle, depth, and beam position. After that, we performed sweeps for each parameter to check the robustness of the result as well as the dependence of the coupling on the angle of incidence, obtaining the values shown in **Figure 1d-h**. The FDTD software simulates the propagation of an electromagnetic pulse that can be used to test the spectral sensitivity of the coupler, due to its intrinsically broadband nature.

For the case of the AFM tip front illuminated we get, from the optimization process, a groove pitch of about 528 nm, confirmed by the momentum conservation law of Equation (1), a duty cycle of  $\approx 0.5$ , appearing to be the less critical parameter, an optimal depth of about 50 nm, and a bandwidth close to 50 nm, as shown in Figure 2d–f.

To summarize, we highlight that we achieve a significant efficiency for all the configurations analyzed when an appropriate groove geometry and extension is chosen. Specifically, the grating period and groove depth optimization at fixed angle of incidence and wavelength launch the SPPs unidirectionally, minimizing power loss into any far field diffraction orders. As expected, a configuration involving a small number of grooves, despite the lower efficiency, has a broader SPP coupling wavelength range, enhancing the grating-mediated spectral information transfer from photons to plasmons and vice versa.

### 3. Hot Electron Setup

After the first insulation of single layer graphene (SLG), a zero bandgap ballistic electrons semiconductor,<sup>[35]</sup> the newborn class of 2D TMD captured much of the attention in material science for their inherently new potentialities to create new bidimensional electronic devices for their peculiar optical and electronic properties.<sup>[36]</sup> Similar to graphene, the number of layer of the final crystal determined the TMD transport properties, spanning progressively from fully 2D transport of single layer to a bulk character once the number of layers increased just of few units. This provided an additional degree of freedom into the production design of nanojunctions with specific properties.<sup>[37]</sup> For instance, going from SLG to a Bernal stacked multilayer opened up a gap in the electron energy distribution due to electronic crosstalk between layers, resulting in a reduction in the zero field conductivity which is quite counterintuitive.<sup>[38]</sup> This property was currently regarded as one of the most intriguing possibilities in the realization of new devices, since the electron coupling at the interface with bulk and multistacked bidimensional materials was similarly affected.<sup>[39,40]</sup> Along this line, recently Wang et al.<sup>[41]</sup> developed a device based on the junction of 1, 3, and 7 layered MoS<sub>2</sub> single crystals and a novel p-type large bandgap semiconductor, tin monoxide (SnO, 0.65–0.7 eV indirect<sup>[42]</sup> and 2.65–2.92 eV direct band gap<sup>[43]</sup>). In the same paper (Figure 6; Figure S4, Supporting Information), EFM measurements showed an asymmetric distribution of the electric field at the MoS<sub>2</sub> edges for different crystal orientations, possibly due to the different terminations at the borders caused by the mechanical exfoliation method used to produce high mobility single crystals.<sup>[38]</sup>

Furthermore, with the integration of resonant plasmonic antennas the possibility to modulate by hot-electron doping the optical properties of single MoS<sub>2</sub> layer was demonstrated, inducing a structural phase transition.<sup>[44]</sup> In this case, MoS<sub>2</sub> lattice coordination changed reversibly from a direct band gap semiconductor to a metallic structure paving the way to realize a new class of active optical devices based on these 2D materials.

Another relevant possibility, offered by the 2D MoS<sub>2</sub> single layer, related to the intense PL was derived by the strong

spin-orbit coupling induced by the valence band splitting. The application of plasmonic structures could control the PL actively. In particular, it was demonstrated that MoS<sub>2</sub> excitons coupled with SPPs could enhance the photoluminescence by more than 10 times and that PL could be further manipulated controlling the optical spin state, or the geometry of applied spiral plasmonic structures, leading to an actively controlled plasmon–exciton interaction nanophotonics device.<sup>[45]</sup>

Recently, a setup based on the generation of SPPs-induced hot electrons at the contact point between an AFM tip and a semiconductor was developed, exploiting a far field laser radiation and collecting the tip-sample current synchronously with the modulation of the laser.<sup>[14]</sup> This set up allowed scanning of the tip on the sample in contact mode while detecting with nanometric resolution the presence of different chemical composition, defects, and junctions.

Due to these particular features, a MoS<sub>2</sub>/SnO junction device was therefore considered as an optimal test bench to verify the sensitivity and the resolution of the setup, with the aim to investigate at the high spatial resolution, the material properties used for the device, and the resulting junctions.

In the following, topography, SKPM, and HENs current measurement are reported together with a comparison with micro-Raman mapping.

#### 3.1. Sample

The investigated device consisted of a 7-layer MoS<sub>2</sub> single crystal/SnO (nominal 15nm) junction, realized according to a procedure described in more details in ref. [41]. The mechanical exfoliated MoS<sub>2</sub> multilayer was transferred on a 300 nm SiO<sub>2</sub>/Si substrate that provides good electrical insulation and high optical contrast by exploiting multiple reflections at the two silicon dioxide interfaces. MoS<sub>2</sub> nanosheets were considered ideal for the photo-electrocatalytic applications because they offer a structure consisting of only surface atoms/edge sites.

A p-type, 15 nm thick, SnO layer was afterward deposited by reactive magnetron sputtering and partially overlapping the MoS<sub>2</sub> multilayer, in order to create the junction. Finally, Ti/Au electrodes were deposited on top of the two sides to provide the electrical connections. Optical and AFM topography images of the device are shown in **Figure 3**.

The sample was connected to the output of the microscope scanning head (Asylum Research MFP3D bio) with a Dual Orca conductive AFM module (dual gain  $G_1 = 10^9 \text{ V A}^{-1}$ , current range  $\pm 10 \text{ nA}$ ;  $G_2 = 10^6 \text{ V A}^{-1}$  current range  $\pm 10 \text{ }\mu\text{A}$ ). An additional resistor ( $R_1 = 108.7 \text{ M}\Omega$ ) was introduced between the sample and the bias source to limit the current from the sample, thus avoiding damages to the gold coating of the tip (Nanosensors ATEC-CONT-Au, nominal spring constant  $0.2 \text{ N m}^{-1}$ ) that might occur at higher voltages. The microscope was equipped with a probe station setup on the scanning stage (Asylum Research, Probe Station), which allowed connecting the limiting resistor directly to one of the gold pads on the p-side of the junction by means of a micromanipulator to obtain a stable Ohmic connection. Photoexcitation at the tip was provided by an external linearly vertically polarized laser (HeNe 633 nm, laser power  $50 \text{ }\mu\text{W}$  at the tip) mechanically modulated at 815 Hz,

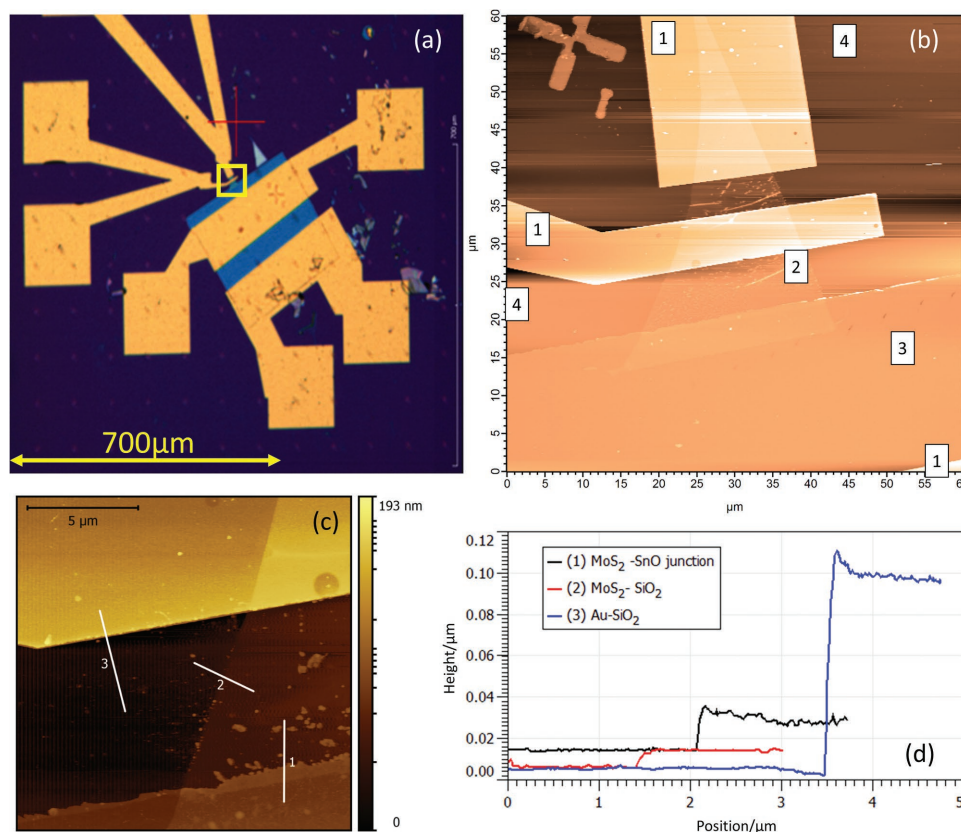


**Figure 3.** a) Optical image of the device. The yellow square corresponds to the junction area, further magnified in the AFM topography data b). The numbered markers indicate the electrodes (1), the MoS<sub>2</sub> (n-type) crystal (2), the SnO p-type film (3), and the SiO<sub>2</sub> substrate (4). c) Higher magnification AFM topography. d) Line profiles of the junction area showing the different height of the electrode, SiO<sub>2</sub>, MoS<sub>2</sub>, and SnO.

aligned and focused on the front side of the tip by an additional optical setup mounted on the microscope antivibration stage (see Section S2 of the Supporting Information for details). This level of power was well below the structural phase transformation for the MoS<sub>2</sub> layer reported in ref. [44]. The scanning design of the microscope and a dedicated temperature/humidity control embedded in the enclosed acoustic hood surrounding the AFM guaranteed a stable alignment of the laser with the tip for a maximum scan range (90 μm × 90 μm) for several hours. The current signal from G<sub>1</sub> was simultaneously acquired by the AFM controller and externally fed to a lock-in amplifier (for further details see Section S2 of the Supporting Information).

Two different acquisition configurations are possible in the setup. In fact, one can measure the high sensitivity G<sub>1</sub> current channel, bringing information on the overall DC and averaged AC current, and the AC photon induced current filtered by the lock-in (with an overall conversion factor from lock-in signal to tip-sample current of  $G_{LIA} = 100 \text{ nA}_{\text{rms}} \text{ V}_{\text{rms}}^{-1}$ ), or the current signal from the G<sub>1</sub> and G<sub>2</sub> gain channels, allowing recording the overall current also in an extended range, according to the measurement requirements. G<sub>1</sub> current and sample bias are also acquired in parallel by an independently controlled fast acquisition system (National Instruments PXI, sampling rate 200 kHz) for the high sampling rate detection and analysis of the signals in the time domain. All the measurements were performed at 29.0 ± 0.1 °C, while the humidity was reduced below 5% RH

by flushing dry air in the acoustically isolated hood, thus preventing electrochemical oxidation or reduction of the sample when a tip-sample bias was applied. Such a phenomenon is known to be mediated by the formation of a water meniscus at the tip-sample interface that occurs at higher relative humidity on most of the materials used in device fabrication.<sup>[46–50]</sup>

## 4. Results

### 4.1. AFM Topography and Kelvin Probe Measurements

Sample topography in correspondence of the junction allows estimating a thickness of  $14 \pm 0.2 \text{ nm}$  for the SnO film, of  $4.2 \pm 0.2 \text{ nm}$  for the MoS<sub>2</sub> crystal, corresponding to 7 layers, and of 90 nm for the Ti/Au electrode (Figure 3).

In this work, we focus our effort in the investigation of MoS<sub>2</sub> surface and crystal edge and on the SnO film with an insight at the junction. MoS<sub>2</sub> is a transition-metal dichalcogenide (TMD) with a direct bandgap of 1.3–1.7 eV, depending on the number of layers and the crystal quality.<sup>[37,51]</sup>

The contact potential of the device and the uniformity of the materials have been verified by SKPM (tip: asylum electrilever, TiIr coating, Nominal Resonance frequency 75 kHz, nominal spring constant 2 N m<sup>-1</sup>, NAP height 30 nm). The contact potential map in Figure 4 demonstrates the chemical uniformity

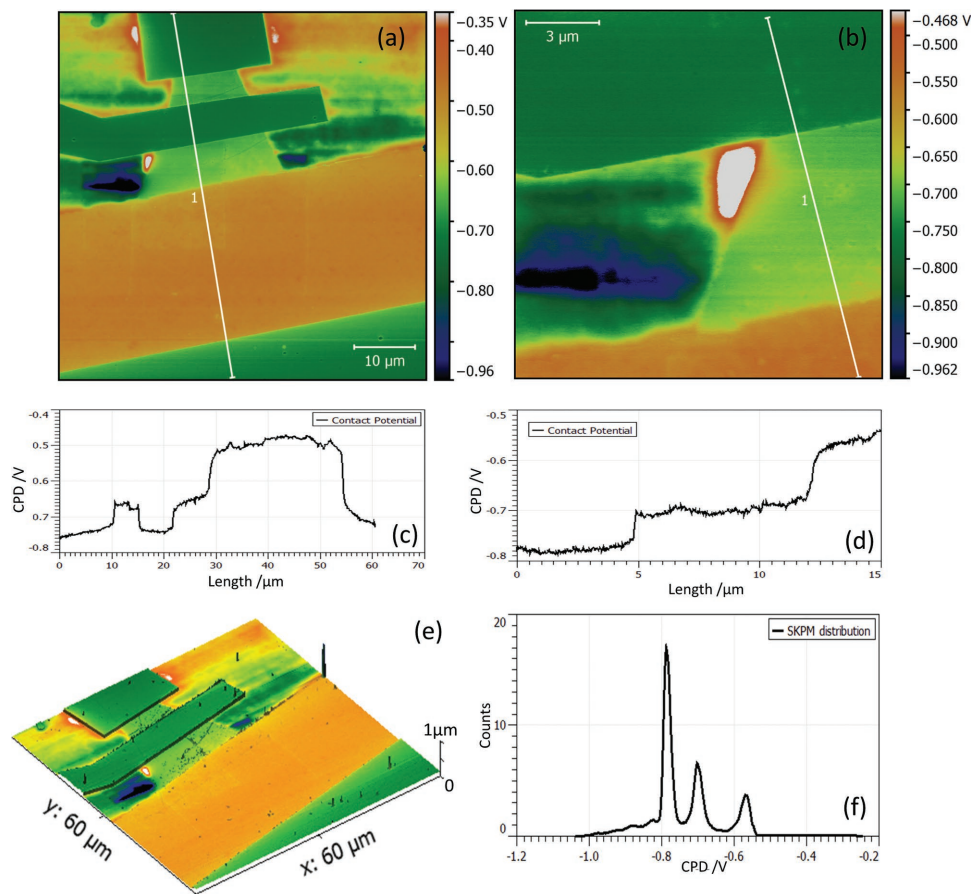


**Figure 4.** Contact potential as measured on the device a) and in correspondence of the junction area b). Line profiles c) and d) corresponding to the cut in (a) and (b), respectively, allow estimating contact properties at the junctions between different materials. e) 3D rendering of the contact potential represented as a color map superimposed over topography data shows the matching between the CPD and the structures. f) Histogram of the contact potential values from image (b) allows measuring the mean value and the FWHM corresponding to each material as reported in the text.

of each material, which does not show any unexpected texture. The histogram of the contact potential differences (CPDs) with respect to the tip is shown in Figure 4. A Gaussian fit of the three peaks gives for Gold  $CPD_{Au} = -786 \pm 22$  mV, for  $MoS_2$   $CPD_{Au-MoS_2} = -86 \pm 30$  mV and  $CPD_{MoS_2-SnO} = -130 \pm 28$  mV. The fit of the line profile across the junction with a smooth bent step model (error function plus second order polynomial) reveals a physical extension of the junction contact potential of 40 nm at the Au/ $MoS_2$  interface and of 200 nm at the  $MoS_2$ /SnO interface. These values are similar to the ones found with electric force microscopy (EFM) technique by Wang et al.<sup>[41]</sup> Within the sensitivity of our SKPM measurements, no differences between the  $MoS_2$  crystal and its edge can be appreciated.

## 4.2. Transport Measurements

A further insight is given by electrical transport measurements in correspondence of  $MoS_2$ , SnO, and their junction. Conductive AFM and current signal filtered by lock-in amplifier were collected both in imaging mode at constant bias and by means of  $I$ - $V$  curves, while the laser is coupled through the grating with the AFM tip scanning the sample surface. Since the energy

of the photons is higher than the bandgap in correspondence of the  $MoS_2$ , the modulated signal is then expected to arise from the combined contribution of hot-carriers generated at the gold-coated tip apex by plasmon decay and photoelectrons generated by direct excitation across bandgap. Hot-electrons are predicted to be generated with a high and stable signal and to provide a contribution to the photocurrent with nanometers spatial resolution.<sup>[14]</sup> **Figure 5** reports measurements performed on  $MoS_2$ . Contact mode topography (acquired at a constant load of 15 nN) on  $MoS_2$  (Figure 5a) shows on the right side an atomically flat uniform area with an RMS roughness of 0.13 nm, representative of very low defective single crystal surface. At the border, an intermediate step characterized by the presence of few fractures and an extension of 10–20 nm can be recognized. A line profile across the edge (Figure 5b,c) indicates that the height of the step is 3.0 nm at the intermediate kink and 4.2 nm at the terrace top, consistent with 5 and 7 layers of  $MoS_2$ , respectively. From the step edge between  $SiO_2$  and the 5-layer  $MoS_2$  parts it is possible to estimate a tip curvature radius below 18 nm.

The total current image (Figure 5d) shows a stable signal in the order of 2.3 nA for an applied sample bias of 0.5 V with a spatial fluctuation of 0.2 nA emerging from the background, revealing features on top of the 7-layer terrace. Interestingly,

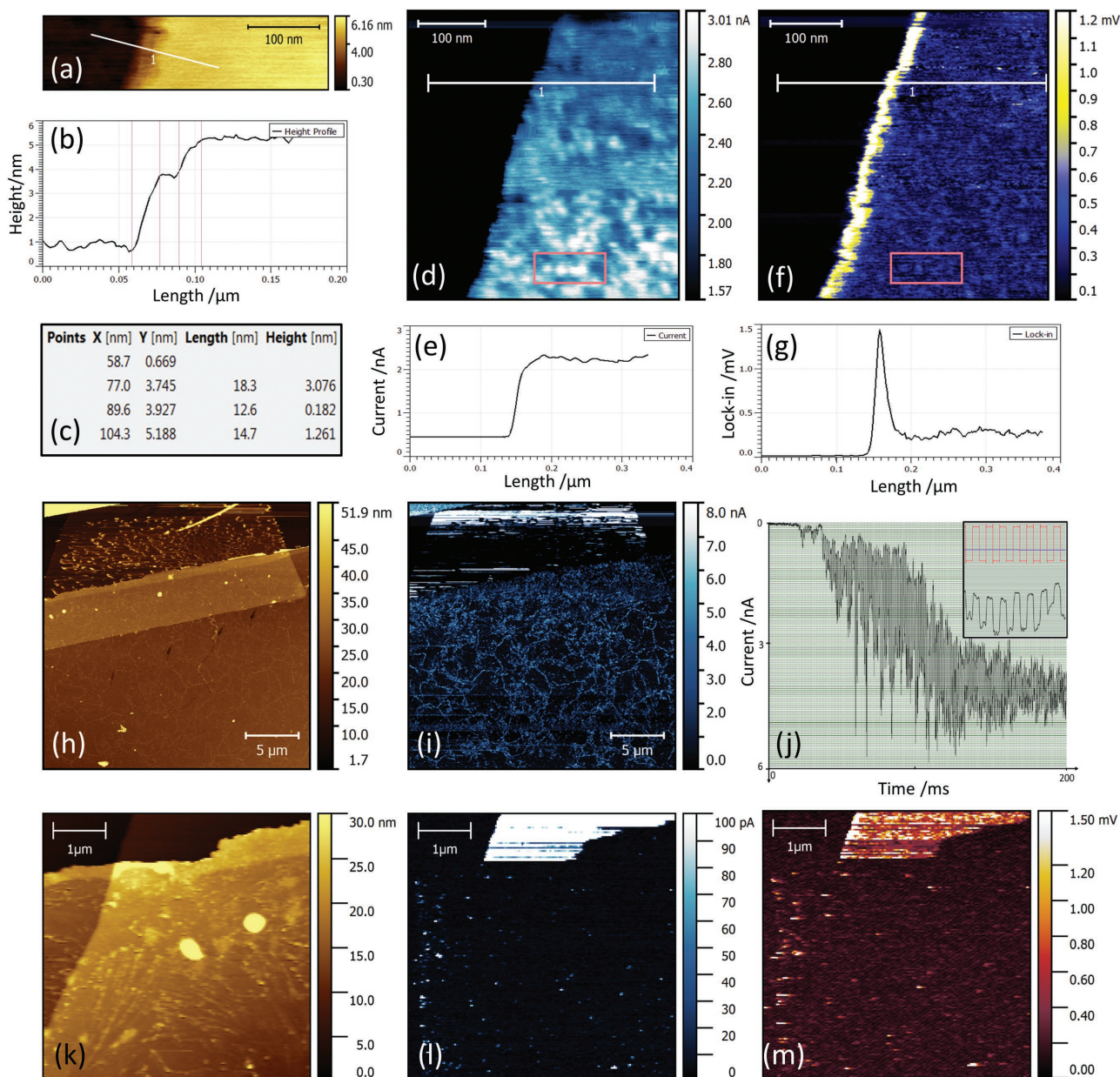


**Figure 5.** a) Contact mode AFM topography at the step edge of the MoS<sub>2</sub> crystal, showing the presence of an intermediate kink. A line profile b) shows the extension and the height of the intermediate step c). d) Total current signal (AC + DC) on the MoS<sub>2</sub> (bright side) with SiO<sub>2</sub> (dark side) at a constant sample bias of 0.5V, and lock-in filtered current signal ( $G_{LIA} = 100 \text{ nA}_{\text{rms}} \text{ V}_{\text{rms}}^{-1}$ ). e) line profile of d) along the white line. f) The AC current signal shows conductance modulations with extension of few tens of nanometers on the MoS<sub>2</sub> surface, as highlighted in the red box. g) Conductance line profile across the step edge of f) along the white line. Comparison between e) and g) shows the difference in the two current signals at the step edge. j) Fast acquisition of the Current signal at the step edge. The AC part is superimposed to the DC part. Topography h,k), total current i,l), and lock-in signal m) of the junction and SnO area at a bias of 3 and 0 V, showing a current contribution at the different grain edges of the polycrystalline SnO.

the same features are found in the trace and retrace image with a complete correlation, demonstrating that they derive from a real modulation in surface conductance. Their average spatial extension turns out to be 20 nm as deduced from the height–height correlation function of the current image on the MoS<sub>2</sub> area. The transition part in correspondence of the step edge, the 5-layer kink, appears smooth, without revealing any distinguishable step-like dependence on the number of layers and punctual fractures within our experimental sensitivity; a slightly

rounded decrease in the conductance at the very step edge with an extension of  $\approx 20$  nm can be explained by a different contact geometry at the border. The lock-in filtered image (Figure 5f) highlights the same features found in the 7-layer region in the total current image (red squares), yet with a higher contrast. This is due to the combined effect of two aspects: first, the line profiles reveal a higher relative change in the lock-in signal (up to 30%, with respect to  $\approx 10\%$  for the total current) in correspondence the 7-layer flat part. Secondly, height–height



correlation function reveals an average dimension of the features of 10 nm, indicating a twofold higher spatial resolution.

Moreover, the current component, which is synchronous with the laser, also shows the appearance of new features. A stark difference emerges at the terrace step all along the crystal border, where the signal (and the conductance for the photo-induced current) is six times higher with respect to the averaged value on top of the 7-layer crystal. It comes up in a narrow region, which is 40 nm large, as indicated by the line profile in Figure 5g, resulting in the more evident difference with the C-AFM conductance discussed before. It is important to mention that the same signal is found regardless of the scan direction, excluding possible topographical cross-talks such as uncontrolled load-induced contact resistance or capacitance change. This feature reveals different junction characteristic in the two investigated areas. We speculate that this can be due to a different nature of the contacts of the tip in the two cases. The MoS<sub>2</sub> nanoplatelets with a triangular shape expose [1010] Mo-edges that are the most active sites, and [1110] sulfur edges.<sup>[52]</sup> This result is also confirmed by Scanning Tunneling Microscopy/Spectroscopy (STM/STS) in Ultra High Vacuum (UHV) measurements where the reconstruction and appearance of electronic modulations at the step edge is demonstrated.<sup>[53]</sup> We observe the edges of the nanoplatelets as bright borders in the lock-in current as well as in the Raman images. The bright borders suggest the presence of an enhanced conductivity at the edge, an effect predicted by Density Functional Theory (DFT) calculations.<sup>[54]</sup> We observe that MoS<sub>2</sub> has a strong conductance anisotropy: the conductivity between two adjacent van der Waals (vdW) bonded S–Mo–S sheets is extremely low with a resistivity that has been measured to be 2200 times larger through the basal planes as compared to that measured along Mo planes.<sup>[55]</sup> This behavior means that the single layer nanoplatelets are an optimal structure compared to a multilayer crystal because electrons only need to be transferred from the contact to the platelets. For this reason, the resistance increases when a multiple layered structure has to be crossed. As a final remark, we infer that the difference is analogous to that observed in the deposition of different metal contact on these materials, as reported in a recent paper.<sup>[56]</sup> There, the contact between a metal and a 2D material is effectively modeled also for a vdW contact by the introduction of a tunneling barrier which in our case can effectively describe the dynamic electrical contact between the tip and the sample, in series to the Schottky junction. In this simple tunneling picture,<sup>[36]</sup> the observed increase in photon synchronous conductance is consistent with a reduction of the barrier extension of 40%. In Figure 5j, we report also the on/off temporal structure of the signal due to SPP decay superimposed to the DC component in correspondence of the step edge. We note here that the direct observation of the temporal modulation allows to identify all the phenomena and the transport regimes, with a visible square wave shaped signal in correspondence of the step edge, synchronous with the modulation and whose extent and localization matches the value measured by lock-in signal at the step edge.

On the SnO side of the device, the measurements show a higher variability of the signal, which is related to the polycrystalline character of the material, as shown by the AFM

topography in Figure 5h,k and highlighted by the current measurement at device bias of +3 V shown in Figure 5i. In particular, the current image shows a texture with a very high contrast in correspondence of the grain border representative of a finite conductance, which drops in correspondence of the central part of the single crystals, having lateral dimensions of the order of few micrometers or below. Remarkably, a current signal in the SnO part is also detected at zero bias, visible in both the total (Figure 5l) and the lock-in filtered current signals (Figure 5m), completely reproducible over 50 different scans, present in trace and retrace and showing a very good correlation between the two different channels. It can be noted that, for SnO the photon-induced transport is expected to be largely dominated by the electron channel since direct excitation from the photon decay channel of the SPPs is precluded by energy conservation on the direct bandgap (3 eV) and momentum conservation in the indirect one (0.6 eV). These considerations explain the high spatial correlation between the total current and lock-in signal, visible in Figure 5l,m and Figure S12b,c (Supporting Information), as well as the signal extent. It can be also noticed that in correspondence of the MoS<sub>2</sub> part in Figure 5l,m (top bright feature) the same behavior discussed for images (Figure 5d,f) is also found at zero bias.

We can retrieve further information from *I*–*V* spectroscopy curves acquired in the region shown in Figure 6a for both the total and the filtered lock-in currents. To better highlight the difference between some representative spectra, MoS<sub>2</sub> (blue box), MoS<sub>2</sub>/SnO junction (green box), and SnO (red box) areas are shown in an extended bias range of ±3 V (Figures 6d–f) selected from the 20 × 20 points map in an area of 6.4 × 6.4 μm<sup>2</sup>, and presented for three different bias values in Figures 6g–i.

To get a further insight at the MoS<sub>2</sub> step edge, a refined map of 40 × 40 points in an area of 400 × 400 nm<sup>2</sup> (blue box) at a reduced ±0.8 V bias was also acquired. It corresponds to a relative distance between two different points of 10 nm, comparable to the tip radius, and sufficient to resolve the different behavior at the step edge detected in the lock-in current map (40 nm extension). For this refined map, a selection of representative curves is shown in Figure 6b, and a current map at –0.8 V bias is shown in Figure 6c. This last comparison shows two different current values in correspondence of the center of the crystal (brown part) and the border (light blue) with a reduction of about a factor two in the current. The spatial extension of the light blue part at the edge is of 4 pixels from the very border. In the two regions, the *I*–*V* curves have two very different behaviors: in the center of the crystal we observe a small band gap (Figure 6b, green curve and Figure 6c, black and blue curves), while a wider gap is found in correspondence of the crystal edge (Figure 6b, red and blue curves and Figure 6c, red curve). This behavior observed for a spatial extension of the 40 nm from the border is consistent with the results derived from Figures 5f and 6c.

Differently, in correspondence of the SnO part (Figure 6f) an overall wider gap in the conductance is always found. A high variability, that is representative of the polycrystalline character of the material, has values between ≈1 and 3.8 V where current maps at different bias show a finite current also in the

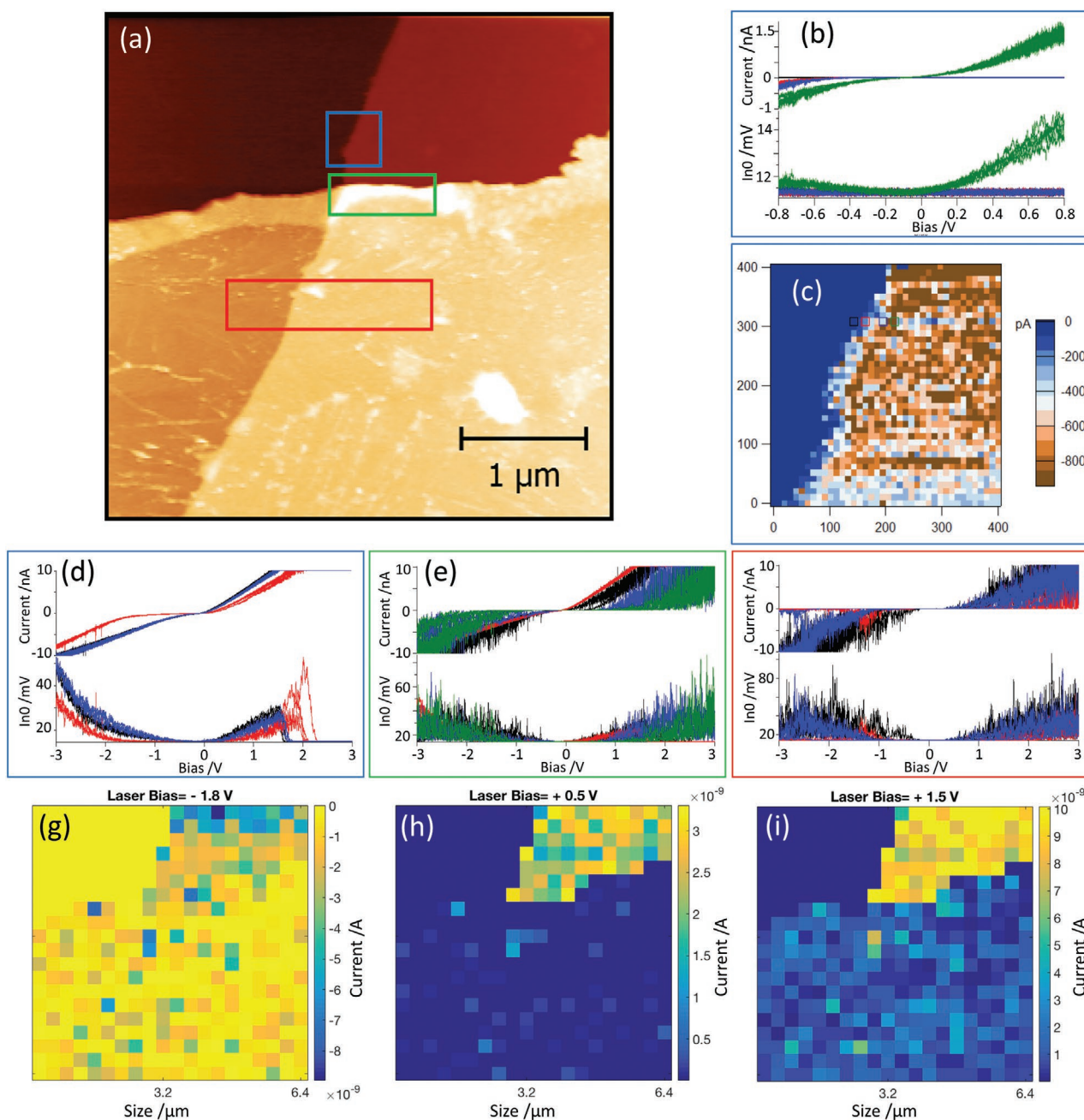


**Figure 6.** a) Topography of the junction region where  $I$ - $V$  spectroscopy is performed. b,d) Current  $I$ - $V$  spectra in correspondence of the  $\text{MoS}_2/\text{SiO}_2$  edge (red and blue) and on top of the crystal (green), both on the total current channel (top) and lock-in one. c) Current Map at constant voltage, showing the difference between top of the crystal (brown) and its edge (light blue).  $I$ - $V$  curves in correspondence of the junction e) and the SnO part f). Maps of the current signal extracted from  $I$ - $V$  curves at g)  $-1.8$  V, h)  $0.5$  V, i)  $1.5$  V showing the spatial distribution in the conductance.

SnO region at low bias of  $-1.8$ ,  $+0.5$ , and  $+1.5$  V, shown in Figures 6g–i, respectively.

At the junction between  $\text{MoS}_2$  and SnO (Figure 6e) both behaviors can be clearly distinguished with a higher variability and mostly on the  $\text{MoS}_2$  side (red and black curves) since they correspond to different locations in the depletion region, whose extension is better highlighted in the map at  $-1.8$  V (Figure 6g), corresponding to an inverse polarization in the p–n junction.

### 4.3. Raman Measurements

We performed confocal Raman mapping and photoluminescence (PL) spectroscopies to evaluate the overall quality of the  $\text{MoS}_2/\text{SnO}$  junction, the homogeneity of the exfoliated  $\text{MoS}_2$  layered surface, the vibrational and excitonic properties for the materials.

A  $50 \mu\text{m} \times 40 \mu\text{m}$  area was mapped by  $150 \times 120$  spectral scans, with a backscattering Raman spectrometer equipped

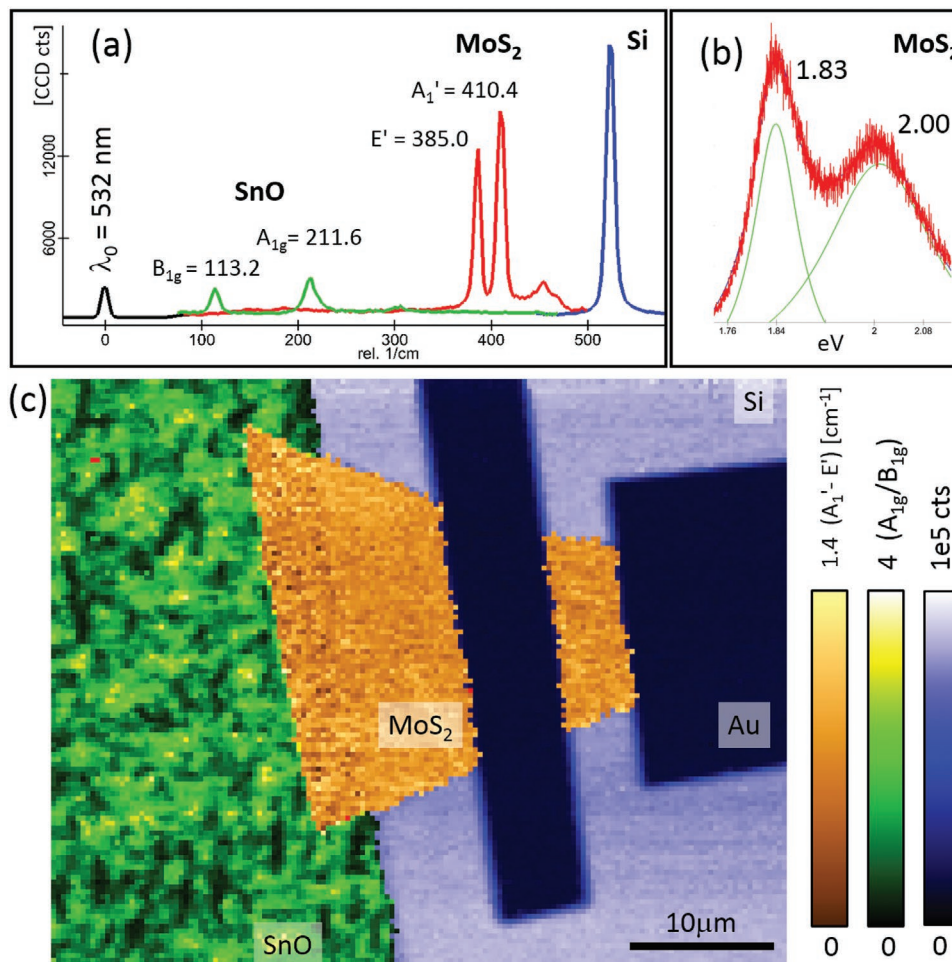


**Figure 7.** Raman and photoluminescence of the hybrid SnO–MoS<sub>2</sub> p–n junction. a) Raman spectra of the representative vibrational modes. SnO Raman active  $B_{1g}$ ,  $A_{1g}$  modes, the  $E'$  and  $A_1'$  modes of 7L MoS<sub>2</sub>, and the silicon peak are shown. b) Photoluminescence (red data) and Lorentzian curve fittings (green lines) of the MoS<sub>2</sub>. An excitation wavelength of 532 nm was used for all Raman and PL spectra. c) Mosaic image composed by different quantities derived from the spectral analysis, as explained in the text.

with 100 $\times$  objective, a grating of 600 grooves  $\text{mm}^{-1}$  and Electron Multiplying Charge-Coupled Device (EMCCD) detector, with an excitation line at 532 nm, considering integration time 1 s per point and a low power level to avoid heating. The effective spectral resolution was  $<9$   $\text{cm}^{-1}$ . In **Figure 7a** we show three typical Raman spectra collected from different areas of the device. The Si Raman band at  $520$   $\text{cm}^{-1}$  was used as an internal frequency reference. Each spectrum was analyzed with five Lorentzian shapes to describe the SnO and MoS<sub>2</sub> material, and the Si, whose spectral contribution was subtracted from the data in the final fitting pass. This procedure allowed evaluating the position, width, and integrated area under the peaks with the nominal spatial resolution of 330 nm.

Following literature assignment for odd-numbered few-layer samples,<sup>[57]</sup> that pertain to the  $D_{3h}$  point group, we indicated the main MoS<sub>2</sub> Raman features at 385 and 410.4  $\text{cm}^{-1}$  as  $E'$  and  $A_1'$ . Both Raman modes exhibit a dependence on thickness,<sup>[58]</sup> meanwhile the frequency of the first mode decreases, that of the second increases with thickness, thus allowing counting the layers number from the peaks separation,  $\Delta f$ , measured along the surface. A  $\Delta f \approx 25.4$   $\text{cm}^{-1}$  corresponds to 7 layers

and confirms the result from the AFM topography profile at the edges of the MoS<sub>2</sub> flake. We report in **Figure 7c** a mosaic map representing different sample properties retrieved from the Raman data analysis, detailed in Section S4 in the Supporting Information. Regarding the MoS<sub>2</sub> it has been plot the  $\Delta f$  quantity with a full-scale intensity of  $1.4$   $\text{cm}^{-1}$ , which allows appreciating the homogeneity of the flake visually within the optical limit. **Figure 7b** shows the MoS<sub>2</sub> PL excitonic peaks that can be assigned to the high energy direct excitonic transition at the K point in the bulk crystal.<sup>[37]</sup> This meaningful behavior of PL emission, visible only in mono or few layers, is absent in bulk MoS<sub>2</sub>, being an indirect bandgap bulk semiconductor like silicon with energy gap about 1 eV. Photoluminescence visibility has been attributed to a dramatically slowing down of the electronic relaxation within the conduction and valence bands in the layered structure, with respect to the bulk. The observed splitting, of about 150 meV, reflects the strong energy split at valence band due to the spin-orbital coupling.

Differently from the MoS<sub>2</sub> flake, the structure of the sputtered SnO film is polycrystalline. Crystallites, with tetrahedral coordination  $D_{4h}^7$ , are preferentially oriented with their  $c$ -axes

perpendicular to the substrate, but randomly oriented within the substrate plane generating the so-called (001)-textured layer.<sup>[59]</sup> Raman scattering spectra show two peaks, one at  $\approx 113\text{ cm}^{-1}$  and the other at  $\approx 211\text{ cm}^{-1}$  corresponding respectively to the Raman active modes  $B_{1g}$  and  $A_{1g}$ , that are the only ones detectable in backscattering geometry for the (001) orientation. A random crystallite orientation in the substrate plane allows any angle between the incident and scattered field directions. Having this in mind, and considering that the  $B_{1g}$  mode gives rise to a scattered field in diagonal as well as for the off-diagonal configuration (i.e., the scattered electric field parallel or perpendicular to the incident electric field), while  $A_{1g}$  mode has essentially diagonal character, is possible to determine the grain size and orientation analyzing the map obtained as  $A_{1g}/B_{1g}$  areas ratio. In our case, we used  $B_{1g}$  as internal reference of the Raman spectrum. The result map is reported in the mosaic Figure 7c. Grains, of microscale size, are in optimal agreement with those determined by AFM topography and current map. We note that the SnO energy gap, in the range 2.5–3 eV, is higher than the excitation line used here, this prevents any photoluminescence observation.

## 5. Discussion and Conclusions

Comparing the experimental results obtained with different techniques, we characterized the two materials at each single region through the junction and Ohmic contacts.

The four techniques, SKPM, C-AFM, HENs, and Raman, supply different experimental quantities related to different surface properties, on comparable spatial lengths but with remarkably different resolution. Micro-Raman is intrinsically limited by the optical diffraction to a lateral resolution in the order of half wavelength ( $\approx 300\text{ nm}$  in our case), SKPM can achieve a resolution in the order of some tens of nanometers, being it limited by the tip to sample distance. HENs, being a nanocontact technique, has an intrinsic spatial resolution at the nanoscale, as it is clear from the images shown in Figure 5.

The combination of these techniques allows a deeper insight into the properties of the device under investigation. SKPM demonstrates that the work function of the different materials is almost uniform, for both  $\text{MoS}_2$  and SnO. This can be clearly seen in Figure 4f, where the width of the histogram of the work function values is peaked around the average values of the materials involved, with a very small dispersion. On the other side, HENs and micro-Raman spectroscopy evidence an inhomogeneity of the samples, revealing much richer details and information. Transport measurement through HENs proves directly that  $\text{MoS}_2$  sample surface has anisotropic conduction characteristics, while SnO has domain arrangement with more conductive edges, all features at the nanoscale that are very interesting for understanding the materials, their electrical behavior and applications.

In particular, for the case of  $\text{MoS}_2$ , AFM topography confirms its monocrystalline nature, while current measurement maps show a variability on both total and lock-in current values, and  $I$ - $V$  curves show nonhomogeneous behavior in the sample as well.

After verifying the reproducibility of the current variation, through a trace and retrace multipass scan, we infer that the current measurements reflect a local variation of the surface state of the material. This conclusion is enforced by the observation that in both, the DC and in the in-phase lock-in demodulated component of the current, we observed fluctuations of the current signal on a length scale of the same order of magnitude. In specific, from  $I$ - $V$  measurement we infer a local variation of the Schottky barrier that would be responsible for this current fluctuation. This local variation can be caused by several different physical effects as the dependence of the band structure on the number of layers, band mixing at the interface, atomic orientational variation of the terminated surface species, such as sulfur atoms,<sup>[60,61]</sup> or defect and dangling bonds charge pinning.

Further significant features in the current signal are found on the borders of the material, where it ends onto the underlying  $\text{SiO}_2$  layer, which is the substrate of the complete device. These borders are where the multilayer of the 2D material is not covered by other materials deposited on top but is completely exposed, giving access to the in-plane structure of the material. In this case a strong lock-in current signal is recorded on the sample and also in this case the current feature is well reproduced in both trace and retrace scanning over the sample and consistent all along the device. We speculate that this is the manifestation of the anisotropic conduction character of this material, which is expected from literature.

On this edge, we observe that the Schottky junction the HEN technique is sensitive provides additional information. Both current measurements in Figures 6b and 5d–g demonstrate a lowering in the DC conductance and a concurrent increase in the photo-induced conductance. The possible cause for this increase is the additional contribution coming from hot carriers to modify the junction and the depletion region or a direct effect of photon absorption that can result in an anomalous photogeneration effect as the one observed in the case of a single monolayer.<sup>[36]</sup> The concurrent reduction in the DC component can be actually attributed to the lower number of  $\text{MoS}_2$  layers at the edge demonstrated by the AFM topographic characterization. The amplitude of this reduction turns out to be smaller than expected,<sup>[41]</sup> since Figure 5d,e plots the total current from the tip to the sample, also including the hot electron contribution, which in this region strongly increases, as described before. The values of the two contributions deduced from the two measurements are in agreement with the current difference which is expected in this case.<sup>[41]</sup> In fact, on this edge the hot electron current injection is favorite because the tip can directly get in contact with the Mo metal material along the highly conducting direction. Differently, the orthogonal contact on the flat top surface of  $\text{MoS}_2$  probes a net reduced conductance because sulfur atoms plane partially shield the electronic  $\text{MoS}_2$  molecular cloud, acting as insulating tunneling barrier.

Raman and photoluminescence spectroscopies on this particular sample do not provide further details, apart from confirming the number of layers and the uniform character of the  $\text{MoS}_2$  surface.

For what concerns the SnO region, AFM topography shows clear features attributable to grain boundaries of the sputtered layer. Interestingly, we observe an overlap between the grain boundaries and the HENs current increase. The current

variation at grain boundary is attributed to the change in the energy band diagram at the interface between two grains of this p-type polycrystalline semiconductor, analogously to what found in literature.<sup>[62,63]</sup> According to the interpretation provided by this literature results, the electrically charged grain boundaries act as hole traps. The current is affected by the capture and emission of holes by the interface states and its modulation derives from a fluctuation of the potential barrier height.<sup>[62,63]</sup>

Photoluminescence and Raman spectroscopies confirm the polycrystalline character of SnO with no variation of chemical composition of the surface. In fact, only relative peak intensities fluctuations are observed on the sample, which can be explained by a conformational variation of the film, while measurements reveal no Raman shift that can be related to a compositional change of the sample, and this turns out to be in perfect agreement with transport measurement provided by HENs.

In summary, by comparing the four spectroscopic techniques, and even confirming a general agreement in the measured quantity, we demonstrated that HEN reveals new features at nanometer scale that shed light on the detailed nature of the semiconductors surfaces. The conduction properties show local fluctuation on a length scale of few tens of nanometers that is attributed to local structural variations of the different materials and that can only be appreciated by means of photoinduced current nanoscopy. We infer that this new features can be due to small variations in junction characteristics, whose experimental confirmation would require a further improvement of our setup with the use of fast laser sources, in line with the numerical simulation on SPP coupling we presented. More extensive experimental studies will be done to confirm and to refine the present findings, including a detailed theoretical analysis to interpret the physics underlying the transport measurements shown in this study. From the experimental point of view, a further improvement is planned by implementing multiwavelength excitation and by collecting contemporarily to the photocurrent also the nano-Raman signal induced by the SPP-to-photon decay channel. Finally, we point out that the new contrast level on the Schottky barrier variation achieved at the edges by HENs, as well as the potential for further improvements can play an important role in understanding the behavior of new interesting systems such as vdW junctions in multistacked 2D materials.

## Supporting Information

Supporting Information is available from the Wiley Online Library or from the author.

## Acknowledgements

This study was funded by KAUST funding grant from office of competitive research: CRG3-2014, "Multipurpose nano spectroscopies with spatial and temporal control through adiabatic compression and localization of surface plasmon polariton."

## Conflict of Interest

The authors declare no conflict of interest.

## Keywords

hot-electrons nanoscopy, MoS<sub>2</sub>-SnO vdW heterojunction, nanoscale characterization, surface plasmon polaritons

Received: March 1, 2017

Revised: April 11, 2017

Published online: June 8, 2017

- [1] M. I. Stockman, *Opt. Express* **2011**, 19, 22029.
- [2] D. K. Gramotnev, S. I. Bozhevolnyi, *Nat. Photonics* **2010**, 4, 83.
- [3] A. O. Govorov, H. Zhang, H. V. Demir, Y. K. Gun'ko, *Nano Today* **2014**, 9, 85.
- [4] A. O. Govorov, H. Zhang, Y. K. Gun'ko, *J. Phys. Chem. C* **2013**, 117, 16616.
- [5] A. Giugni, B. Torre, M. Allione, G. Perozziello, P. Candeloro, E. Di Fabrizio, *Conductive Atomic Force Microscopy: Applications in Nanomaterials*, M. Lanza, Wiley-VCH, Weinheim, **2017**.
- [6] T. Gong, J. N. Munday, *Opt. Mater. Express* **2015**, 5, 2501.
- [7] M. A. Ordal, R. J. Bell, R. W. Alexander, L. L. Long, M. R. Querry, *Appl. Opt.* **1985**, 24, 4493.
- [8] A. B. Petrin, *Quantum Electron.* **2015**, 45, 658.
- [9] A. B. Petrin, *Quantum Electron.* **2016**, 46, 159.
- [10] A. B. Petrin, *High Temp.* **2016**, 54, 475.
- [11] M. I. Stockman, *Phys. Rev. Lett.* **2004**, 93, 137404.
- [12] M. I. Stockman, *Phys. Rev. Lett.* **2011**, 106, 019901.
- [13] D. K. Gramotnev, M. W. Vogel, M. I. Stockman, *J. Appl. Phys.* **2008**, 104, 034311.
- [14] A. Giugni, B. Torre, A. Toma, M. Francardi, M. Malerba, A. Alabastri, R. P. Zaccaria, M. I. Stockman, E. Di Fabrizio, *Nat. Nanotechnol.* **2013**, 8, 845.
- [15] A. O. Govorov, H. Zhang, *J. Phys. Chem. C* **2015**, 119, 6181.
- [16] R. Sundararaman, P. Narang, A. S. Jermyn, W. A. Goddard III, H. A. Atwater, *Nat. Commun.* **2014**, 5, 5788.
- [17] M. L. Brongersma, N. J. Halas, P. Nordlander, *Nat. Nanotechnol.* **2015**, 10, 25.
- [18] B. Y. Zheng, H. Zhao, A. Manjavacas, M. McClain, P. Nordlander, N. J. Halas, *Nat. Commun.* **2015**, 6, 7797.
- [19] X.-C. Ma, Y. Dai, L. Yu, B.-B. Huang, *Light Sci. Appl.* **2016**, 5, e16017.
- [20] W. Li, Z. J. Coppens, L. Vázquez, W. Wang, A. O. Govorov, J. Valentine, presented at *Frontiers in Optics 2015*, San Jose, California, October **2015**.
- [21] A. B. Petrin, *High Temp.* **2012**, 50, 15.
- [22] R. Proietti Zaccaria, A. Alabastri, F. De Angelis, G. Das, C. Liberale, A. Toma, A. Giugni, L. Razzari, M. Malerba, H. B. Sun, E. Di Fabrizio, *Phys. Rev. B* **2012**, 86, 035410.
- [23] H. Raether, *Surface Plasmons on Smooth and Rough Surfaces and on Gratings*, Vol. 111, Springer, Berlin **1988**.
- [24] U. Fano, *J. Opt. Soc. Am.* **1941**, 31, 213.
- [25] S. A. Maier, S. R. Andrews, L. Martín-Moreno, F. J. García-Vidal, *Phys. Rev. Lett.* **2006**, 97, 176805.
- [26] S. A. Maier, *Plasmonics: Fundamentals and Applications*, Springer Science + Business Media LLC, New York **2007**.
- [27] N. Vasilantonakis, M. E. Nasir, W. Dickson, G. A. Wurtz, A. V. Zayats, *Laser Photonics Rev.* **2015**, 9, 345.
- [28] E. Kretschmann, *Opt. Commun.* **1972**, 5, 331.
- [29] J. J. Foley IV, H. Harutyunyan, D. Rosenmann, R. Divan, G. P. Wiederrecht, S. K. Gray, *Sci. Rep.* **2015**, 5, 9929.
- [30] R. L. Olmon, B. Slovick, T. W. Johnson, D. Shelton, S.-H. Oh, G. D. Boreman, M. B. Raschke, *Phys. Rev. B* **2012**, 86, 235147.
- [31] A. Alabastri, S. Tuccio, A. Giugni, A. Toma, C. Liberale, G. Das, F. De Angelis, E. Di Fabrizio, R. P. Zaccaria, *Materials* **2013**, 6, 4879.
- [32] Z. Shuzhang, T. Tamir, *IEEE J. Quantum Electron.* **1993**, 29, 2813.

- [33] J. Wuenschell, H. K. Kim, *Optics Express* **2006**, *14*, 10000.
- [34] P. Lalanne, J. P. Hugonin, J. C. Rodier, *Phys. Rev. Lett.* **2005**, *95*, 263902.
- [35] K. S. Novoselov, A. K. Geim, S. V. Morozov, D. Jiang, Y. Zhang, S. V. Dubonos, I. V. Grigorieva, A. A. Firsov, *Science* **2004**, *306*, 666.
- [36] W. J. Yu, Q. A. Vu, H. Oh, H. G. Nam, H. L. Zhou, S. Cha, J. Y. Kim, A. Carvalho, M. Jeong, H. Choi, A. H. C. Neto, Y. H. Lee, X. F. Duan, *Nat. Commun.* **2016**, *7*, 13278.
- [37] A. Splendiani, L. Sun, Y. Zhang, T. Li, J. Kim, C.-Y. Chim, G. Galli, F. Wang, *Nano Lett.* **2010**, *10*, 1271.
- [38] A. C. Neto, F. Guinea, N. M. Peres, K. S. Novoselov, A. K. Geim, *Rev. Mod. Phys.* **2009**, *81*, 109.
- [39] X. Wang, F. Xia, *Nat. Mater.* **2015**, *14*, 264.
- [40] L. Britnell, R. Ribeiro, A. Eckmann, R. Jalil, B. Belle, A. Mishchenko, Y.-J. Kim, R. Gorbachev, T. Georgiou, S. Morozov, *Science* **2013**, *340*, 1311.
- [41] Z. Wang, X. He, X. X. Zhang, H. N. Alshareef, *Adv. Mat.* **2016**, *28*, 9133.
- [42] W. Zhou, N. Umezawa, *Phys. Chem. Chem. Phys.* **2015**, *17*, 17816.
- [43] J. A. Caraveo-Frescas, P. K. Nayak, H. A. Al-Jawhari, D. B. Granato, U. Schwingenschlöggl, H. N. Alshareef, *ACS Nano* **2013**, *7*, 5160.
- [44] Y. Kang, S. Najmaei, Z. Liu, Y. Bao, Y. Wang, X. Zhu, N. J. Halas, P. Nordlander, P. M. Ajayan, J. Lou, Z. Fang, *Adv. Mater.* **2014**, *26*, 6467.
- [45] Z. Li, Y. Li, T. Han, X. Wang, Y. Yu, B. Tay, Z. Liu, Z. Fang, *ACS Nano* **2017**, *11*, 1165.
- [46] P. Avouris, T. Hertel, R. Martel, *Appl. Phys. Lett.* **1997**, *71*, 285.
- [47] R. Garcia, A. W. Knoll, E. Riedo, *Nat. Nanotechnol.* **2014**, *9*, 577.
- [48] M. Lorenzoni, A. Giugni, E. Di Fabrizio, F. Pérez-Murano, A. Mescola, B. Torre, *Nanotechnology* **2015**, *26*, 285301.
- [49] M. Lorenzoni, B. Torre, *App. Phys. Lett.* **2013**, *103*, 163109.
- [50] M. Lorenzoni, A. Giugni, B. Torre, *Nanoscale Res. Lett.* **2013**, *8*, 75.
- [51] Q. H. Wang, K. Kalantar-Zadeh, A. Kis, J. N. Coleman, M. S. Strano, *Nat. Nanotechnol.* **2012**, *7*, 699.
- [52] A. B. Laursen, S. Kegnaes, S. Dahl, I. Chorkendorff, *Energy Environ. Sci.* **2012**, *5*, 5577.
- [53] J. V. Lauritsen, J. Kibsgaard, S. Helveg, H. Topsoe, B. S. Clausen, E. Laegsgaard, F. Besenbacher, *Nat. Nanotechnol.* **2007**, *2*, 53.
- [54] H. Zhong, R. Quhe, Y. Wang, Z. Ni, M. Ye, Z. Song, Y. Pan, J. Yang, L. Yang, M. Lei, J. Shi, J. Lu, *Sci. Rep.* **2016**, *6*, 21786.
- [55] H. Tributsch, *Ber. Bunsengesellschaft Phys. Chem.* **1977**, *81*, 361.
- [56] A. Allain, J. Kang, K. Banerjee, A. Kis, *Nat. Mater.* **2015**, *14*, 1195.
- [57] K. H. S. Kirby, D. E. Chris, V. S. Saurabh, P. Eric, *2D Mater.* **2017**, *4*, 011009.
- [58] C. Lee, H. Yan, L. E. Brus, T. F. Heinz, J. Hone, S. Ryu, *ACS Nano* **2010**, *4*, 2695.
- [59] J. Geurts, S. Rau, W. Richter, F. J. Schmitte, *Thin Solid Films* **1984**, *121*, 217.
- [60] E.-D. Fung, O. Adak, G. Lovat, D. Scarabelli, L. Venkataraman, *Nano Lett.* **2017**, *17*, 1255.
- [61] K. Wu, J. Chen, J. McBride, T. Lian, *Science* **2015**, *349*, 632.
- [62] A. Carbone, P. Mazzetti, *Phys. Rev. B* **1998**, *57*, 2454.
- [63] H. H. Güttler, J. H. Werner, *Appl. Phys. Lett.* **1990**, *56*, 1113.